Vacancy and interstitial interactions with crystal/amorphous, metal/covalent interfaces

Sanket S. Navale*, Michael J. Demkowicz

Department of Materials Science and Engineering, Texas A&M University, College Station TX, 77843.

Abstract

We use atomistic simulations to investigate the interaction of vacancies and interstitials with interfaces between a crystalline metal and an amorphous, covalently-bonded solid. We select the gold (Au)/silicon (Si) binary system as a model material and construct interface models along two different facets of crystalline Au and with amorphous Si (a-Si) created at three different quench rates. We compute formation energies of vacancies, self-interstitials, and interstitial impurities as a function of position relative to the interface and find that they have markedly lower values near the interface than in the interior of the adjoining phases. We conclude that crystal/amorphous, metal/covalent interfaces may be as effective at removing radiation-induced point defects as interfaces in polycrystalline metals composites. Moreover, irrespective of interface character, the average formation energies of all point defects at all the Au/a-Si interfaces we investigated are comparable. Thus, unlike in polycrystalline metals, where an interface's crystallographic character has a marked effect on its interactions with point defects, all interface types in crystal/amorphous, metal/covalent composites may be equally effective at absorbing all radiation-induced defects.

* Corresponding author: nsanketnavale@gmail.com

1 Motivation

Layered composites of crystalline, metallic α-iron (Fe) and amorphous, covalently-bonded silicon oxycarbide (SiOC) have exhibited remarkable radiation resistance [1,2]. Because their constituent layers have ~100nm-level thickness, these materials contain a high area per unit volume of interfaces between Fe and SiOC [3,4]. Similar to other nanocomposite materials [5], interfaces in Fe/SiOC multilayers are thought to elevate radiation resistance by attracting, absorbing, and annihilating radiation-induced point defects, such as vacancies, self-interstitials, and impurities. However, to date, defect-interface interactions have been studied primarily in the context of materials composed exclusively of crystalline constituents [6]. The interactions of radiation-induced point defects with interfaces between crystalline and amorphous solids—especially covalently-bonded amorphous solids—remain comparatively unexplored. The present study advances understanding of the interaction between radiation-induced point defects and metal/covalent, crystal/amorphous interfaces.

Motivated by the success of atomistic simulations in elucidating interface/defect interactions in polycrystalline metals [7–10], our goal is to carry out an analogous atomistic modeling study of defect interactions with crystal/amorphous, metal/covalent interfaces. A major obstacle is the limited availability of classical potentials. Thus, previous atomistic modeling studies on Fe/SiOC interfaces were performed using first principles methods [11–13]. However, detailed experimental characterization of Fe/SiOC interfaces has revealed that the adjacent constituents react with each other, forming an intermixed layer as thick as 13nm [14]. The high thickness and complex chemistry of Fe/SiOC interfaces [15,16] calls for models that are too large to be amenable to investigation using first principles codes such as VASP [17,18]. Thus, in view of the large model sizes required and lack of suitable classical potentials, atomistic simulations of defect interactions with Fe/SiOC interfaces are infeasible by currently available methods.

In view of the foregoing, we decided to carry out an atomistic study on a model system containing interfaces between crystalline gold (Au) and amorphous silicon (Si). While such a study cannot replace atomistic simulations of Fe/SiOC interfaces, our hope is that it will nevertheless provide qualitative insights concerning the behavior of crystal/amorphous, metal/covalent interfaces in general. Au and Si do not form compounds and exhibit limited solid solubility up to the solidus [19]. Thus, thanks to the relative simplicity of its chemistry, the Au-Si binary is adequately represented with a previously constructed modified embedded atom method (MEAM) classical potential [20], based on single-element MEAM potentials for Au [21] and Si [22]. Our research approach is analogous to one where experimentalist researchers use surrogates, such as CeO_2, in studies on nuclear materials, such as PuO_2, due to difficulties associated with working with the latter [23]. In both cases, a surrogate or "model system" is investigated because the system of actual interest in nuclear applications is beyond the capabilities of currently available methods.

Using the LAMMPS code [24], we calculate point defect formation energies as a function of distance from crystal Au/amorphous Si (a-Si) interfaces and find that these interfaces are potent sinks for vacancies, self-interstitials, and interstitial impurities originating from the interior of either one of the

two adjoining phases. Moreover, irrespective of the type of Au facet at the interface or the quench rate used to create a-Si, the mean formation energies of point defects are comparable at all Au/a-Si interfaces. We conclude that such interfaces may be as effective at removing radiation-induced point defects as interfaces in polycrystalline metals composites. In the following sections, we describe the construction and characterization of our Au/a-Si interface models, present our approach for computing and analyzing defect formation energies, and discuss our results in the context of developing radiation-resistant crystalline/amorphous composites.

2 Model construction

To create a-Si models, we use a melting-and-quenching approach similar to that in Ref. [25]. We start with a crystalline diamond cubic structure at 0 K containing 50,000 Si atoms in a 10 Å x 25 Å x 25 Å orthogonal simulation cell under periodic boundary conditions. We melt the crystal by heating it up to 3500 K using a Nosé-Hoover type NPT ensemble [26,27] with zero external hydrostatic pressure. The liquid is held at 3500 K for 100 ps before cooling down in a three-stage quench, again under zero pressure. In the first stage, we cool the molten Si to 2000 K at a rate of 3.5×10^{12} K/s. In the second stage of cooling, from 2000 K to 1500 K, we choose one of three different rates: QR1 = 7×10^{10} K/s, QR2 = 5×10^{11} K/s, or QR3 = 3.5×10^{12} K/s. During this stage, the molten Si vitrifies into a-Si. In the last stage, we cool the newly formed a-Si to 0 K at a rate of 3.5×10^{12} K/s, performing potential energy minimization (PEM) to relax the structure into its nearest inherent state. According to Stillinger and Weber [28,29], the total number of such states scales as $N!\,e^{\nu N}$, where N is the number of atoms and ν is an unknown positive number. Thus, even for small atomistic models, this number is so large that no two quenches carried out independently are likely to ever fall into the same inherent state. However, consistent with the law of large numbers, the variance of intensive physical quantities, such as the mass or energy density, is expected to scale as $N^{-1/2}$, i.e. variance decreases with model size and large models follow a consistent mean behavior.

All the quench rates used in stage two give rise to distinct glass transition temperatures in the ~1640 – 1760 K range. The characteristic signature of this transition is a rapid increase in the average atomic volume per atom during cooling, as shown in Fig. 1. Slower cooling rates lead to sharper transitions at higher temperatures and with a larger volume per atom in the final, vitrified state. These observations are consistent with previous simulations of a-Si formation during rapid quenching from the melt [25,30]. However, they contrast with the behavior of metallic glasses, which typically exhibit lower volumes per atom for slower cooling rates. This difference is due to the fact that liquid Si is denser than crystalline Si while molten metals are typically less dense than their corresponding crystalline states.

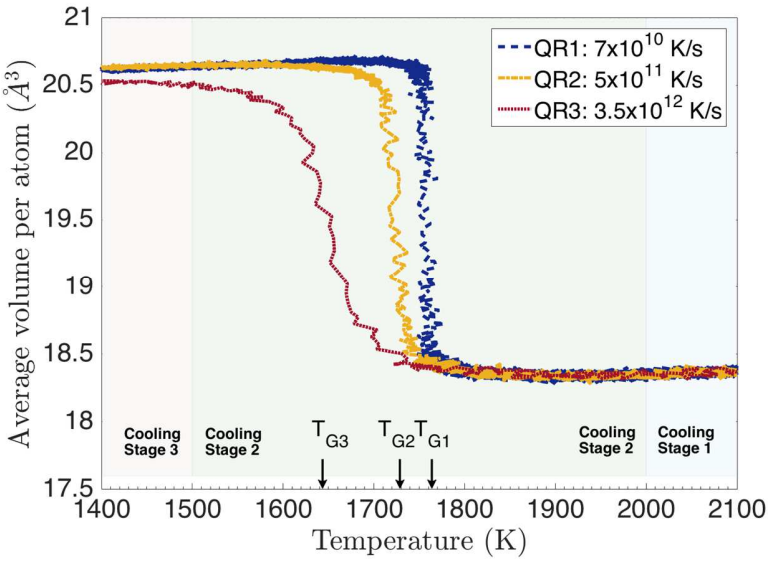

Fig. 1: The average volume per atom of Si exhibits a rapid increase at the glass transition temperature during stage two of cooling.

Fig. 2 shows radial distribution functions (RDFs) for the a-Si structures obtained using the three aforementioned quench rates along with a RDF for diamond cubic Si at 0 K, for comparison. The lack of distinct peaks past a distance of ~6Å for QR2 and QR3 demonstrates a loss of translational long-range order in these models, consistent with a fully amorphous structure. The RDF for QR1 shows some similarity to the peak structure of the reference crystalline material, yet again without long-range order beyond ~7Å, suggesting that the model may consist of small crystalline domains embedded in an amorphous matrix.

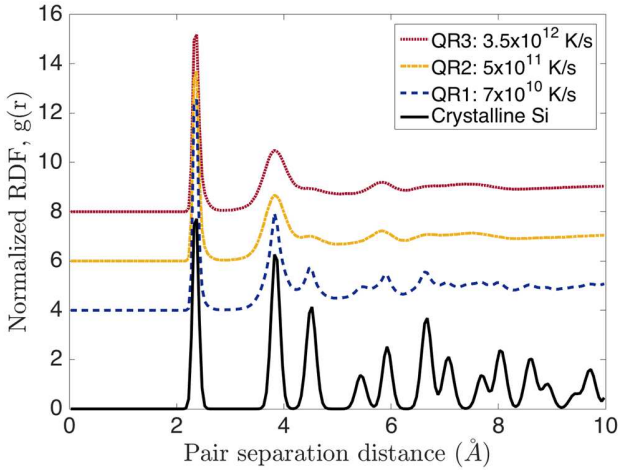

Fig. 2: Radial distribution functions (RDFs) of a-Si created with three quench rates and of diamond cubic crystalline Si at 0 K. For clarity, the a-Si RDFs have been offset by integer increments.

To characterize the local atomic environments in our models, we perform common neighbor analysis (CNA) using the OVITO code [31]. Fig. 3 shows the distribution of atomic structure types for models created using the three different quench rates. As expected from the RDF data, the model created using QR1 contains clusters of atoms whose local structure is diamond cubic or diamond hexagonal. These clusters account for ~24% of the total model volume with the majority of the remainder being

non-crystalline. The models with higher quench rates only contain small, isolated groups of atoms with diamond cubic or diamond hexagonal local ordering, consistent with the structure being fully amorphous. Table I summarizes the findings of this CNA analysis of a-Si structure.

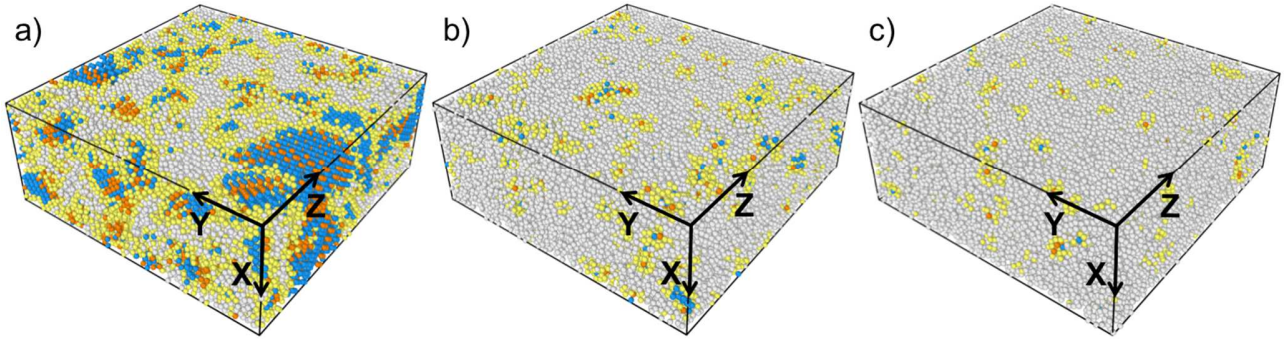

Fig. 3: Atomic structure of a-Si models created with quench rates a) QR1, b) QR2, and c) QR3. The atomic environments of atoms colored blue have diamond cubic crystal structures. Orange atoms are locally diamond hexagonal. Yellow atoms connote defective regions within those lattices. White atoms are not associated with any identifiable crystal structure.

Table I: Crystal structure analysis in a-Si structures.

Crystal type ↓ \Quench rate →	**QR1 (%)**	**QR2 (%)**	**QR3 (%)**
Diamond Cubic (Blue)	15.8	1.9	0.5
Diamond Hexagonal (Orange)	8.5	1.4	0.5
Defective atoms in diamond lattices (Yellow)	42.8	20.7	11
Other atoms (White)	32.9	76	88

To create models of Au/a-Si interfaces, we join individual a-Si structures to a layer of crystalline Au. The dimensions of the Au layers in the interface plane are chosen to match the dimensions of the a-Si layers to within 1% error, i.e., leading to < 1% misfit strain after joining and relaxation of the simulation cell. We create Au layers with two different interface facets, namely {111}- and {112}-type. The former is a close-packed plane often associated with low energy interfaces in metal composites [32,33]. The latter is more corrugated, with nanometer-scale steps. In metal composites, it is associated with higher-energy interfaces found in materials processed by severe plastic deformation [34].

Given two different Au facets and a-Si structures formed by three different quench rates, we have six distinct Au/a-Si interface models. These models have periodic boundary conditions in the interface plane and free surfaces in the direction normal to the interface (x-direction). To relax these models, we perform a room temperature (RT) anneal at 300 K and relax the structure to its nearest inherent state using potential energy minimization *via* the conjugate gradient method [35,36]. During the relaxation, model dimensions are allowed to adjust to yield zero external pressure. All relaxed models have misfit stresses lower than 400 MPa in both Au and a-Si layers.

We compute the energies of Au/a-Si interfaces with area A_{int} as

$$\gamma_{int}^{avg} = \frac{E_{total} - n_{Au}E_{Au}^{coh} - n_{Si}E_{Si}^{coh}}{A_{int}} \quad (1)$$

where E_{total} is sum of atomic energies within a 50 Å-thick region centered on the interface, n_{Au} and n_{Si} are the numbers of Au and Si atoms contained in the region, E_{Au}^{coh} is the cohesive energy per atom of crystalline Au, and E_{Si}^{coh} is the average cohesive energy per atom of a-Si at the quench rate used to build the model. Because periodic boundary conditions are applied parallel to the interface plane, A_{int} is determined by the model dimensions along the y- and z-directions. Table II summarizes the cohesive energies used in this calculation.

Table II: Cohesive energy values of Au and Si in different structures.

Material	Crystalline Au	Crystalline Si	a-Si @QR1	a-Si @QR2	a-Si @QR3
Cohesive energy per atom (eV)	-3.93	-4.63	-4.44	-4.38	-4.36

The computed interface energies are plotted in Fig. 4. These energies span a range comparable to interfaces found in metal heterophase interfaces, such as in Cu/Nb composites [34,37,38], as well as grain boundaries (GB) in metals such as Ni or Al [39]. As expected, {111}-type Au facets result in interface energies that are systematically lower than the {112}-type facets. The energies vary non-monotonically with a-Si quench rate. The relatively high energy of the interface with a-Si created using QR1 is due to the presence of a disproportionate number of crystalline regions away from the interface that contribute to the E_{Si}^{coh} term, but not necessarily in the E_{total} term of Eqn. 1.

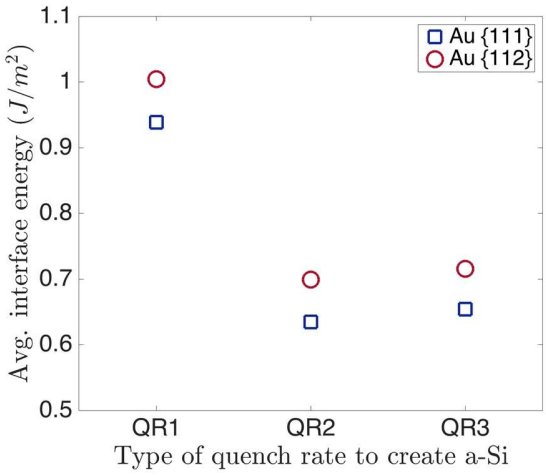

Fig. 4: Energies of Au/a-Si interfaces with different Au facets and a-Si quench rates.

As means of validation, we also compute point defect formation energies in perfect crystal fcc Au and diamond cubic Si using the MEAM potential and compare them to literature, as summarized in Table III. Since we use a classical potential for our simulations, we restrict ourselves to considering only uncharged defects in Si. We are not able to find any reliable experimental data on self-interstitials in Au. Furthermore, the available first principles modeling studies on Au self-interstitials are thirty or more years old and should be taken with caution. The computed values for vacancy formation energies in crystalline Au closely match with those reported in first principles modeling studies and experiments. In contrast, the vacancy formation energies for crystalline Si are lower by ~1eV than those reported in the literature and higher by ~0.2-1eV for self-interstitials studied by first principles (albeit there is still considerable disagreement between calculations and experiments on Si

interstitials). These discrepancies preclude quantitatively accurate predictions of point defect energies, but do not diminish our ability to explore qualitative trends in point defect behavior, which is the goal of the present study.

Table III: Vacancy and interstitial formation energies (eV) in perfect crystal bulk Au and Si.

Defect Type			**MEAM potential**	**First principles calculations**	**Experiment**
Vacancy	Au		0.91	0.82 [40]	0.93 [41], 0.89 [42]
	Si		2.35	3.33 [43], 3.31 [44]	3.6 [45]
Self-interstitial	Au in Au	tetrahedral	3.54	4.0 – 5.5 [46–48]	N/A
		octahedral	2.81	2.7 – 4.1 [46–48]	
		[100] split dumbbell	2.81	2.1 – 3.8 [46–48]	
	Si in Si	tetrahedral	5.45	4.51 [49]	3.18 [50], structures unknown
		[100] split dumbbell	4.67	N/A	
		[110] split dumbbell	N/A	4.46 [49]	
Interstitial impurity	Au in Si	tetrahedral	7.04	N/A	N/A
		[100] split dumbbell	6.56		
	Si in Au	tetrahedral	2.52	N/A	N/A
		octahedral	2.09		
		[100] split dumbbell	2.81		

3 Point defect formation energies at Au/a-Si interfaces

For each interface model, we compute formation energies of point defects as a function of position relative to the interface, extending out to a distance of 25 Å on both sides of the interface plane. The subsections below describe our findings for three types of defects: vacancies, self-interstitials, and interstitial impurities (i.e., Au interstitials in Si and Si interstitials in Au).

3.1 Vacancies

We compute ~100,000 vacancy formation energies in Au ($E_{vac}^{f,Au}$) and Si ($E_{vac}^{f,Si}$) in all interface models. In each calculation, we delete one atom from a configuration initially free of point defects (with energy

$E_{initial}$), relax the modified structure using conjugate gradient PEM in LAMMPS, and calculate the energy E_{final} of the equilibrated model. We determine the vacancy formation energy as

$$E_{vac}^{f} = (E_{final} + E_{coh}) - E_{initial}, \quad (2)$$

where E_{coh} is the cohesive energy of the deleted atom, as provided in Table II. Following Ref. [38,51], we only relax atomic positions within a spherical region of radius 20 Å centered on the vacancy site. All atoms outside this region are held fixed during the relaxation. We confirmed that this approach yields identical vacancy formation energies as when the entire model is relaxed. However, the reduction in the simulation domain size provides many-fold acceleration of the computation and allows for the completion of ~1000 formation energy calculations on a single CPU in one day.

Fig. 5 shows the atomic structure of the interface model with (111)-Au facet and a-Si created using QR1, and, just below it, a plot of E_{vac}^{f} as a function of distance to the interface, with the interface plane located at the origin. The mean, standard deviation, and standard error for both $E_{vac}^{f,Au}$ and $E_{vac}^{f,Si}$ are plotted over the raw data, also as functions of distance from the interface. A 5 Å bin width is used to compute these quantities. Bounds defined by the standard errors are so narrow that they are essentially coincident with the means. As-constructed (vacancy-free) interface models contain some Au atoms that have displaced into the adjacent a-Si layer during relaxation. Whenever fewer than six of the nearest neighbors of such an atom are Au atoms, we consider its removal to be equivalent to the creation of a Si vacancy. The formation energies for all such vacancies are computed the same way as for all other Au atoms and shown by black diamond markers in Fig. 5. However, when computing means and standard deviations of formation energies, these values are counted along with Si vacancies in our analysis. We define an analogous criterion for distinguishing whether a deleted Si atom creates a Si vacancy or an Au vacancy (purple star markers in Fig. 5).

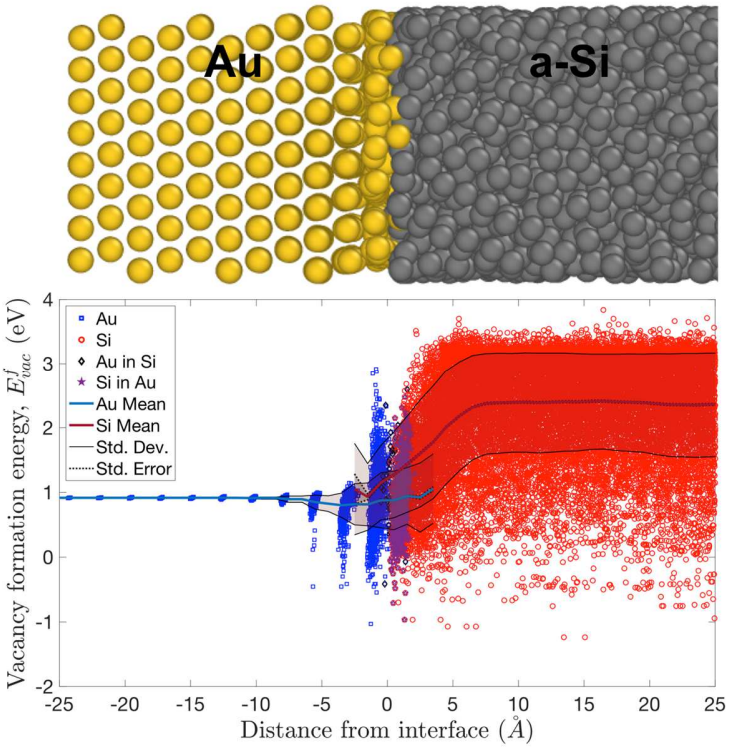

Fig. 5: Top: a (111)-Au/a-Si (QR1) interface. Bottom: vacancy formation energies plotted as a function of distance from the interface. Superimposed on the raw data are means, standard deviations, and standard errors of the vacancy formation energies, also computed as functions of distance from the interface. Blue markers/curves are for Au vacancies; red are for Si vacancies.

Far from the interface, all values of $E_{vac}^{f,Au}$ (E_{vac}^{f} in the Au layer) are equal to the vacancy formation energy in perfect crystalline, face centered-cubic (fcc) Au: 0.91 eV [40–42]. By contrast, there is substantial scatter of $E_{vac}^{f,Si}$ (E_{vac}^{f} in the a-Si layer) due to the amorphous structure of the Si layer. For the model shown in Fig. 5, the mean value of $E_{vac}^{f,Si}$ far from the interface is 2.4 eV, close to the vacancy formation energy in diamond cubic crystalline Si: 2.35 eV (see Table III). In other interface models, $E_{vac}^{f,Si}$ converges to different mean values far from the interface plane.

There is also marked scatter in E_{vac}^{f} (for both Au and Si vacancies) near the interface plane. The mean values of both $E_{vac}^{f,Au}$ and $E_{vac}^{f,Si}$ are lower near the interface than in the interiors of the Au and a-Si layers. The mean curve for a-Si, shown by solid red line, is lower by ~1 eV at the interface compared to the interior of the layer while the reduction in the mean for Au (in blue) is relatively weaker, in the range of 0.1-0.2 eV. For both Au and Si vacancies, there are numerous interface sites with negative E_{vac}^{f}, indicating that the interface contains numerous annihilation sites for vacancies originating from either of the adjacent layers.

The qualitative features shown in Fig. 5 are also seen in all other Au/a-Si interface models that we investigated. Thus, in Fig. 6 we plot only the mean E_{vac}^{f} curves for all these models. The mean $E_{vac}^{f,Au}$ curves are almost coincident across all interface models, with no dependence on the exposed Au facet, as expected. In contrast, the mean $E_{vac}^{f,Si}$ curves in Fig. 6 converge to different values away from the interface, depending on the quench rate, i.e., degree of crystallinity. The difference between mean energy in a-Si and crystalline Si increases as the degree of crystallinity in a-Si decreases. Thus, a-Si created using QR3 contains more sites of high energy and low free-volume, where vacancies form with greater ease, i.e., lower formation energy. Interestingly, average vacancy formation energies near the interfaces are nearly equal at ~1eV regardless of the quench rate used to make the a-Si layer. Thus, defect interactions with Au/a-Si interfaces appear to be insensitive to the structure of the amorphous layer far from the interface. They are also insensitive to the index of the Au facet parallel to the interface plane.

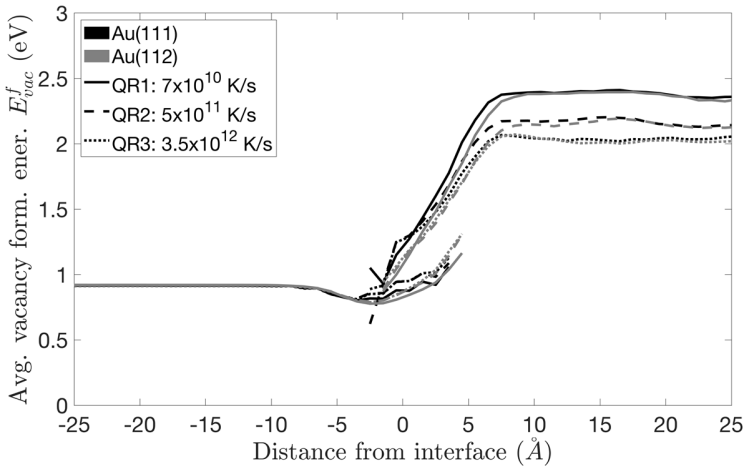

Fig. 6: Mean vacancy formation energies as a function of position relative to the interface plane in different Au/a-Si interface models.

3.2 Self-interstitials and interstitial impurities

We create interstitials by inserting atoms at predefined locations on a grid with a spacing of 1 Å: about one quarter of the lattice parameters of Au and Si. This way, the tetrahedral, octahedral, and other lattice voids in both materials are sampled. Interstitial formation energies, E_i^f, are computed as,

$$E_i^f = E_{final} - (E_{initial} + E_{coh}), \tag{3}$$

with cohesive energy values taken from Table II, as before. To relax configurations containing interstitials, we employ a procedure similar to the one described for vacancies. In particular, we restrict the simulation domain to a spherical region of radius 20 Å centered at the location of inserted atom. As before, we verified that the formation energies computed this way are the same as when a full structure relaxation is performed. The inserted atom is categorized as self-interstitial atom (SIA) when the atom and host lattice are of the same element. When the atom and host lattice are different elements, then the defect is classified as an interstitial impurity.

Fig. 7 presents the formation energies of Au interstitials. Fig. 7.a) plots all data for the interface model with a (112)-Au facet and a-Si created using QR2, along with the superimposed statistical curves. The blue square markers in left half of the plot correspond to Au SIAs while the right half shows Au interstitial impurities in Si, marked as red circles. Fig. 7.b) plots the $E_i^{f,Au}$ mean curves in all interface models. In the Au layer, the SIA formation energies far from the interface equal that of the [100]-split dumbbell in fcc Au, as reported in Table III. By inspecting the structure of these defects, we confirmed that they are indeed [100]-split dumbbells. In the a-Si layer, the interstitial impurity formation energies stabilize far from the interface at values equal to or greater than the formation energy of the [100]-split dumbbell SIA in Au. These values depend on the quench rate of the a-Si layer, with lower quench rates yielding higher formation energies.

The interface has a strong effect on Au self-interstitials, reducing $E_i^{f,Au}$ on average by 2 eV and creating significant scatter in energies, extending ~15 Å into the Au layer. In the a-Si layer, the mean $E_i^{f,Au}$

saturates within ~5 Å from the interface. Compared to vacancies, there are many more interstitial sites at and near the interface with negative $E_i^{f,Au}$.

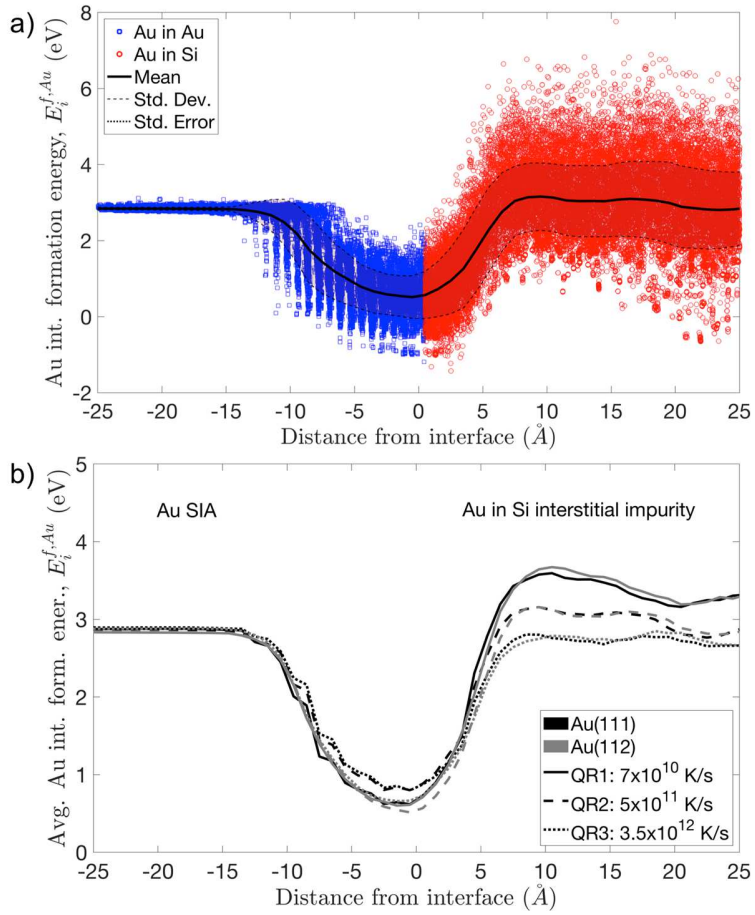

Fig. 7: Formation energy of Au interstitials as a function of distance to the interface plane. a) Scatter plot for (112)-Au/a-Si (QR2) interface model with superimposed statistical curves. Blue markers are for Au self-interstitials; red are for Au interstitial impurities in a-Si. b) Mean energy curves in all the Au/a-Si interface models. Vertical dashed-dot line represents the nominal position of interface.

Fig. 8 presents the data on Si interstitials, with the left half of both plots displaying formation energies of Si interstitial impurities in Au and right half Si SIAs. Fig. 8.a) is a plot for the interface model with a (111)-Au facet and a-Si created using QR3, together with superimposed statistical curves. It is evident from the separation of Si interstitial impurity energies (blue square markers) into three bands far from the interface in Fig. 8.a) that these defects have three stable configurations in Au, as reported in Table III. Si SIA energies saturate far from the interface, with the average energy depending on the quench rate of the a-Si.

At the interface, $E_i^{f,Si}$ values are reduced by ~1 eV, compared to the interiors of the adjoining layers, with the influence of the interface extending ~10 Å in both directions. There are numerous sites at the interface and across the entire a-Si layer with negative $E_i^{f,Si}$. Fig. 8.b) plots mean $E_i^{f,Si}$ curves in all interface models, exhibiting the same trends as in Fig. 8.a).

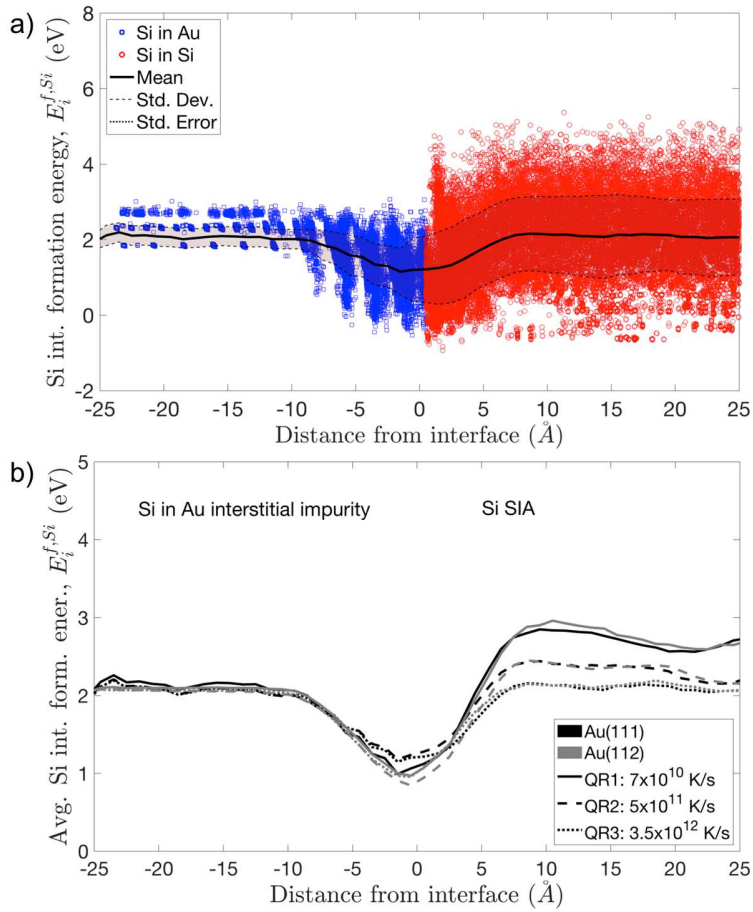

Fig. 8: Formation energy of Si interstitials as a function of distance to the interface plane. a) Scatter plot for (111)-Au/a-Si (QR3) interface model with superimposed statistical curves. Blue markers are for Si interstitial impurities in Au; red are for Si self-interstitials. b) Mean energy curves in all the Au/a-Si interface models. Vertical dashed-dot line represents the nominal position of interface.

The data shows that E_i^f for both types of interstitials are lowered—and, in many individual cases, negative—near the Au/a-Si interfaces, demonstrating that these interfaces are good sinks for interstitials. The interfaces have a stronger effect on Au interstitials, as seen from the larger drop in formation energies in Fig. 7.b) compared to Fig. 8.b). E_i^f in a-Si, away from interface, depends on the quench rate used to create the a-Si. The a-Si created with QR3 consistently shows lower E_i^f, likely due to the higher energy and lower free volume of these structures.

Nevertheless, similar to the case of vacancies, the quench rate of the a-Si layer does not affect interstitial formation energies at the interface itself. Similarly, the index of the Au facet at the interface does not appear to have any effect on E_i^f. Indeed, both Au and Si self-interstitials and interstitial impurities all have formation energies of ~1eV at all the interfaces studied here.

3.3 Interface structure analysis

The foregoing calculations show that point defects of all types (vacancy, self-interstitial, interstitial impurity) have the same formation energies of ~1eV at all the Au/a-Si interfaces, irrespective of the Au

facet index and a-Si quenching history. To better understand the origin of this confluence, we investigate the local atomic environment near the interfaces using the analysis method described in Ref. [25]. This technique examines the distribution of angles between nearest neighbor bonds for each atom in an a-Si structure. For every a-Si atom in a given model, we compute the mean (μ) and standard deviation (σ) of these bond angles. Fig. 9.a) plots μ against σ for each Si atom in the structure cooled at QR3. This analysis unambiguously separates the a-Si atoms into ones with 'solid-like' and 'liquid-like' local environments, as proposed by Demkowicz and Argon [25,30]. The solid-like atoms can be described as segments of a continuous random network (CRN) [52], which has the same topological environment and coordination numbers for each a-Si atom as diamond cubic crystalline Si.

We quantify the mass fraction of solid-like atoms and plot it against the quench rate used to create each a-Si structure. The data exhibits a linear relationship in Fig. 9.b) when a logarithmic scale is used for the quench rate. The mass fraction of solid-like atoms increases with decreasing quench rate, further indicating that the a-Si created with QR1 is structurally more similar to crystalline Si than QR2 or QR3.

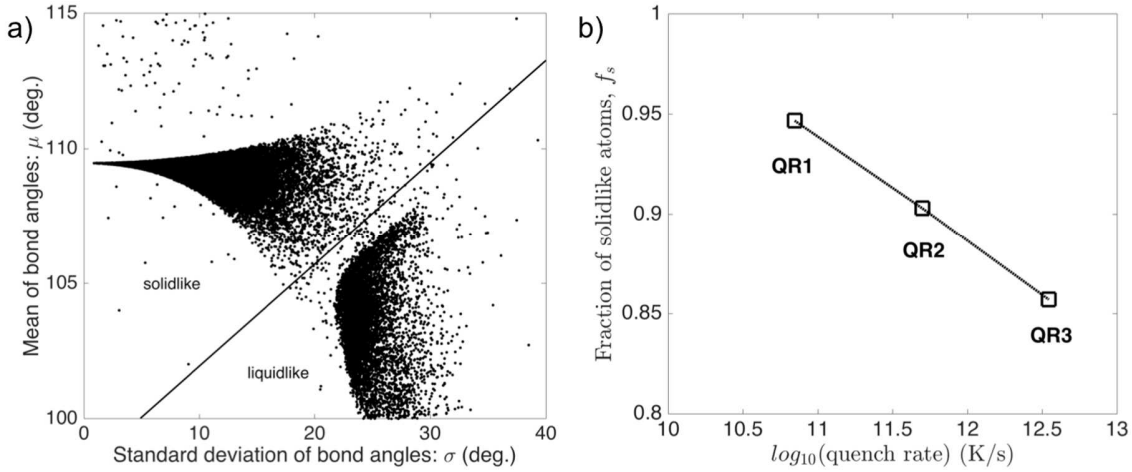

Fig. 9: a) Plotting the mean, μ, against the standard deviation, σ, of bond angles for every atom reveals a clear separation of local atomic environments into two types: solid-like and liquid-like [25,30]. b) The fraction of atoms with solid-like atomic environments increases with decreasing quench rate.

Applying the above analysis to our interface models, we compute the mass fraction of solid-like atoms in a-Si, now as a function of distance from the interface. Fig. 10 plots the computed mass fraction of solid-like atoms in each interface model, demonstrating an unambiguous drop in solid-like atom fraction near the interface (X=0). Far away from the interface, the curves saturate to values shown in Fig. 9.b). To the extreme right of Fig. 10, the curves abruptly drop again as they reach the free surface of a-Si in their respective structures. This drop can be attributed to the dangling bonds of a-Si atoms at the free surface and reflects the abrupt change in the local atomic environment.

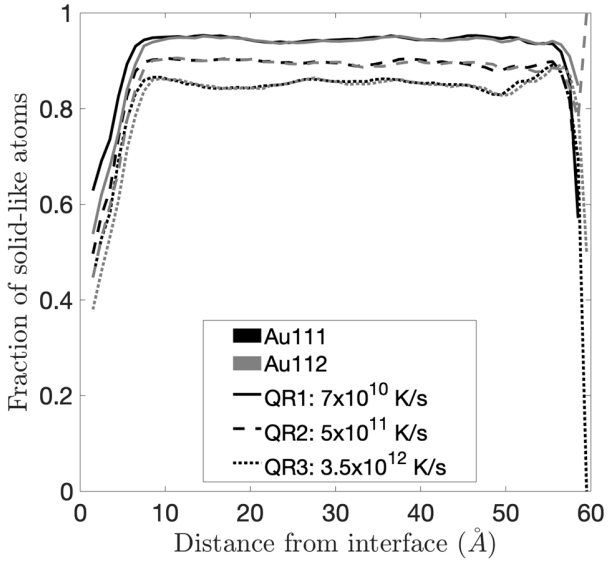

Fig. 10: Fraction of solid-like atoms in the a-Si layer as a function of distance from the interface.

Finally, Fig. 11 shows the average formation energy of defects as a function the average solid-like mass fraction in all of our interface models. For all defect types, formation energies decrease as the mass fraction of solidlike atoms decreases, confirming a direct proportionality between these two quantities. Moreover, at the lowest values of solidlike mass fraction in each model, all defect formation energies reach the same, ~1eV levels. Nevertheless, the plots of defect formation energy vs. solidlike mass fraction do not overlap across the entire plotted range. Thus, while solidlike mass fraction accounts for qualitative trends in defect formation energies, a fully quantitative relation requires additional or different structural descriptors.

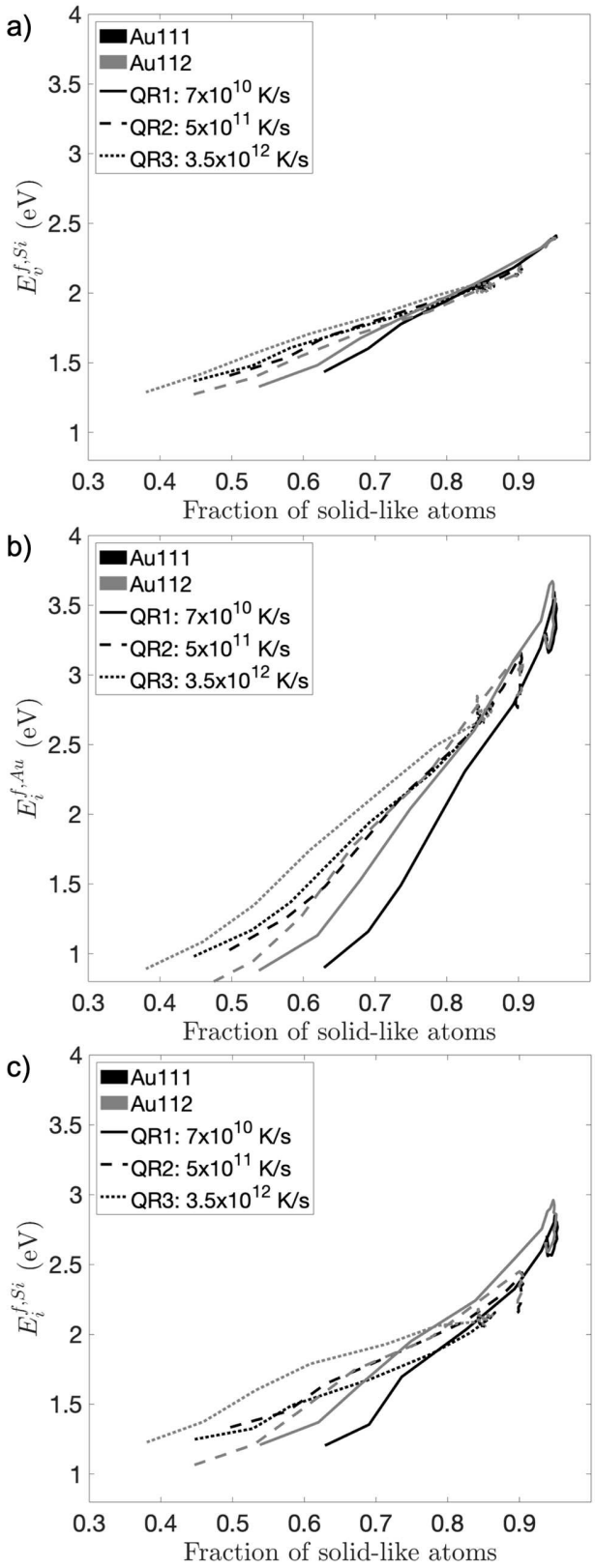

Fig. 11: Average defect formation energy as a function of fraction of solid-like atoms in the a-Si layer: a) vacancies, b) Au interstitial impurities, c) Si self-interstitials.

4 Discussion

We constructed six atomic models of crystalline Au/amorphous Si interfaces using two different crystal facets of Au and three different quench rates for forming a-Si. We characterized the amorphous structure of Si using radial distribution functions, common neighbor analysis, and bond angle analysis. We also calculated formation energies for vacancies, self-interstitials, and impurity interstitials as a function of distance from the interface for all the models. For all six interface models, we found that the formation energies of these defects are significantly lower at the interface than in the adjacent layers. Furthermore, due to the consistently low fraction of solid-like a-Si atoms at the interfaces, all point defects have comparable, ~1eV formation energies at all interfaces, irrespective of interface character and defect type (vacancy, self-interstitial, interstitial impurity). Thus, we conclude that Au/a-Si interfaces are potent sinks for point defects and exhibit the same interactions with them, independent of the exposed Au facet or the quench rate used to create a-Si.

Similar to previous studies [25], we build models of a-Si by quenching liquid Si at rates of 7×10^{10} - 3.5×10^{12} K/s. This quench rate is many orders of magnitude higher than that used in the fabrication of other amorphous solids, such as metallic glasses [53]. However, in experimental investigations, a-Si is not made through quenching because liquid Si crystallizes far too readily. Instead, a-Si may be made either through vapor deposition [54], shock compression [55], or heavy ion bombardment [56]. Performing faithful simulations of these processes is beyond the scope of the current work. However, we argue that the quenching rates used in our study are a reasonable way to make a model a-Si structure. To support this view, we observe that a-Si formation by heavy ion bombardment occurs through the rapid melting and quenching of crystalline Si in localized thermal spikes induced by ion collision cascades [57]. As has been shown in previous studies [58], the quench rate of a liquid in a thermal spike is on the order of 10^{13} K/s. The quench rates used in our study (7×10^{10} - 3.5×10^{12} K/s) are comparable and, in fact, lower than this value. Our most rapidly quenched model is approximately 2.3% less dense than diamond cubic Si while a-Si made by self-ion bombardment is ~1.8% less dense than diamond cubic Si [56]. The difference between the calculated and measured densities may be due to the lower quench rate used in our simulations, compared to thermal spike quench rates in irradiated solids. However, it may also be due to shortcomings in the Si potential used in this study [22] or the simplicity of the model, which does not account for impurities commonly encountered in a-Si, such as hydrogen [59].

Our findings on Au/a-Si interfaces exhibit similarities to previous investigations on interfaces in single- and multi-phase polycrystals. Multiple studies have shown that interfaces between crystalline solids are effective traps for radiation-induced point defects [7,60]. Our work demonstrates that metal/covalent, crystal amorphous interfaces are similarly effective as defect sinks. Thus, increasing the area per unit volume of either type of interface in composite materials provides additional potential sites for the removal of radiation-induced defects [5]. One key difference between crystal/crystal interfaces and crystal/amorphous interface is that the former are expected to contain no negative defect formation energy sites when properly equilibrated [61–63]. However, this expectation rests on the fact that the crystalline solids that meet at the interface are themselves at (or near) thermodynamic equilibrium.

By contrast, amorphous materials, such as a-Si, are far from thermodynamic equilibrium [53]. Consequently, the interfaces they form with other materials cannot be expected to be near

thermodynamic equilibrium, either. a-Si in fact does not meet the most basic thermodynamic definition of a phase: it does not correspond to a minimal free energy state, whether global or local. Rather, it is a thermodynamically unstable (as opposed to metastable) state that relaxes continuously (albeit, under some conditions, rather slowly) towards ever lower energies until it crystallizes. Roorda et al. used differential isothermal calorimetry to demonstrate that, regardless of preparation route, a-Si undergoes continuous relaxation up until the point of crystallization [64].

The fact that a-Si cannot be considered a well-defined phase in the usual thermodynamic sense has important consequences for the formation of defects. If a defect is introduced into any solid that is at a free energy minimum (whether local of global), then the overall energy of the solid must increase and the defect must have positive formation energy. However, a defect introduced into a thermodynamically unstable solid can either increase or decrease the energy of that solid, depending on how or where the defect is introduced. Consequently, its energy can be positive or negative. Indeed, in Fig. 5, which shows vacancy formation energies throughout the entire a-Si layer, even regions that are far from the interface contain negative vacancy formation energy sites. Such sites are an inherent feature of far-from-equilibrium matter, of which a-Si is an example.

Finding an amorphous material of any composition that may be considered a genuine, thermodynamically stable phase is one of the longest-standing research topics in the field of amorphous solids. It began with the foundational work of W. Kauzmann [65] and culminated in the working definition of an “ideal glassformer” proposed by C. A. Angell [66]. To date, only two amorphous materials have been found to fulfill this criterion: atactic polyvinylacetate [67] and certain non-aqueous calcium-nitrate electrolytes [68]. In particular, no examples of single-element ideal glassformers have been reported. The properties of point defects in ideal glassformers have yet to be investigated.

Previous investigations have shown that the radiation response of interfaces between crystalline solids depends on the crystallographic character of the interface [69–71]. For example, highly coherent interfaces are poorer sinks than interfaces with more disordered internal structures [72]. Even for interfaces with similar structures, differences between their long-range stress fields may cause significant discrepancies in sink strength [73]. Thus, the development of radiation-resistant crystalline composites requires achieving control over the interface character distribution [74]. By contrast, defect formation energies at the crystal/amorphous interfaces investigated here do not exhibit any dependence on the interface character, including the exposed facet of the crystalline component and the quenching history of the amorphous component. This insensitivity may prove be a general characteristic of metal/covalent, crystal/amorphous interfaces, including those found in Fe/SiOC composites [1,2]. It is beneficial for the development of radiation-resistant crystal/amorphous composites, as it obviates the need to control interface character.

In the present study, the ability of Au/a-Si interfaces to trap defects was explained by reference to the structure of the a-Si material close to the interfaces. Specifically, we showed that the fraction of solid-like atoms near the interfaces is significantly lower than in the interior of the a-Si layer. Thus, the difference in bonding and structure between the Au and a-Si reduces atomic ordering at the interface, allowing for easier accommodation of point defects. This finding contrasts with previous work by Brandl et al. on interfaces between crystalline and amorphous metals [75]. They found that the metallic amorphous material close to those interfaces shows a tendency towards greater structural

ordering, compared to the interior of the crystalline layer. Thus, it appears that crystal/amorphous interfaces may exhibit markedly different structures depending on whether or not there is a change in the type of boding across the interface, i.e. whether the interface is a metal/metal or a metal/covalent interface.

There remain many open questions about point defect behavior and radiation response of crystal/amorphous interfaces. For example, our investigation did not inquire into the mechanisms by which high-energy particles create point defects in a-Si nor whether or how these defects later migrate or react with other defects. Furthermore, the present study focused on determining the formation energies of removed or added atoms (i.e., vacancies or interstitials, respectively). However, it did not characterize the structure of the final relaxed configurations. Point defect structure is well defined for crystalline materials due to their long-range order [41]. Its definition and characterization is problematic in amorphous materials because of the lack of long-range order. Thus, previous descriptions of point defects in amorphous metals typically relate them to excess free volume [76] and often refer to them 'vacancy-like' or 'interstitial-like' defects [77]. However, vacancies in amorphous silicon appear to have more definite structures, largely thanks to the relative stability of these defects over microsecond-scale times [78]. The structures of interstitials in a-Si and other covalent amorphous materials remain to be explored.

5 Acknowledgements

This work was supported by the U. S. Department of Energy, Office of Nuclear Energy, Nuclear Energy Enabling Technologies (NEET) Reactor Materials program, under contract No. DE-NE0000533. We are grateful to M. Nastasi for helpful discussions. The High-Performance Research Computing (HPRC) center at Texas A&M University provided the computational resources required for this work.

6 Data Availability

The raw data required to reproduce these findings are available to download at https://doi.org/10.5281/zenodo.3723326.

7 References

[1] Q. Su, L. Price, L. Shao, M. Nastasi, J. Nucl. Mater. 479 (2016) 411.
[2] Q. Su, L. Price, L. Shao, M. Nastasi, Metals (Basel). 6 (2016) 261.
[3] Q. Su, L. Price, L. Shao, M. Nastasi, Mater. Res. Lett. 4 (2016) 48.
[4] Q. Su, L. Price, J.A.C. Santana, L. Shao, M. Nastasi, Mater. Lett. 155 (2015) 138.
[5] I.J. Beyerlein, A. Caro, M.J. Demkowicz, N.A. Mara, A. Misra, B.P. Uberuaga, Mater. Today 16 (2013) 443.
[6] I.J. Beyerlein, M.J. Demkowicz, A. Misra, B.P. Uberuaga, Prog. Mater. Sci. 74 (2015) 125.
[7] A. Misra, M.J. Demkowicz, X. Zhang, R.G. Hoagland, JOM (2007) 62.
[8] E.G. Fu, A. Misra, H. Wang, L. Shao, X. Zhang, J. Nucl. Mater. 407 (2010) 178.
[9] N. Li, E.G. Fu, H. Wang, J.J. Carter, L. Shao, S. a. Maloy, a. Misra, X. Zhang, J. Nucl. Mater. 389 (2009) 233.
[10] X.M. Bai, A.F. Voter, R.G. Hoagland, M. Nastasi, B.P. Uberuaga, Science 327 (2010) 1631.
[11] H. Ding, M.J. Demkowicz, Sci. Rep. 5 (2015) 1.

[12] H. Ding, M.J. Demkowicz, Acta Mater. 136 (2017) 415.
[13] P. Kroll, J. Mater. Chem. 20 (2010) 10528.
[14] Q. Su, M. Zhernenkov, H. Ding, L. Price, D. Haskel, E.B. Watkins, J. Majewski, L. Shao, M.J. Demkowicz, M. Nastasi, Acta Mater. 135 (2017) 61.
[15] Q. Su, L. Price, L. Shao, M. Nastasi, Scr. Mater. 113 (2016) 79.
[16] Q. Su, J. Jian, H. Wang, M. Nastasi, Philos. Mag. 95 (2015) 3876.
[17] G. Kresse, J. Hafner, Phys. Rev. B 47 (1993) 558.
[18] G. Kresse, J. Furthmüller, Phys. Rev. B 54 (1996) 11169.
[19] T.B. Massalski, J.L. Murray, L.H. Bennett, H. Baker, Binary Alloy Phase Diagrams, American Society for Metals, 1986.
[20] J. Godet, C. Furgeaud, L. Pizzagalli, M.J. Demkowicz, Extrem. Mech. Lett. 8 (2016) 151.
[21] B.J. Lee, J.H. Shim, I. Baskes, Phys. Rev. B - Condens. Matter Mater. Phys. 68 (2003).
[22] B.-J. Lee, Comput. Coupling Phase Diagrams Thermochem. 31 (2007) 95.
[23] H.S. Kim, C.Y. Joung, B.H. Lee, J.Y. Oh, Y.H. Koo, P. Heimgartner, J. Nucl. Mater. 378 (2008) 98.
[24] S. Plimpton, J. Comput. Phys. 117 (1995) 1.
[25] M.J. Demkowicz, A.S. Argon, Phys. Rev. B - Condens. Matter Mater. Phys. 72 (2005) 1.
[26] S. Nosé, J. Chem. Phys. 81 (1984) 511.
[27] W.G. Hoover, Phys. Rev. A 31 (1985) 1695.
[28] F.H. Stillinger, T.A. Weber, Phys. Rev. A 28 (1983) 2408.
[29] F.H. Stillinger, T.A. Weber, Science (80-.). 225 (1984) 983.
[30] M.J. Demkowicz, A.S. Argon, Phys. Rev. Lett. 93 (2004) 025505.
[31] A. Stukowski, Model. Simul. Mater. Sci. Eng. 18 (2009) 015012.
[32] M.J. Demkowicz, R.G. Hoagland, J. Nucl. Mater. 372 (2008) 45.
[33] X. Zhang, E.G. Fu, A. Misra, M.J. Demkowicz, JOM 62 (2010) 75.
[34] M.J. Demkowicz, L. Thilly, Acta Mater. 59 (2011) 7744.
[35] E. Polak, G. Ribiere, Rev. Fr. d'informatique Rech. Oper. 3 (1969) 35.
[36] M.R. Hestenes, E. Stiefel, J. Res. Nat. Bur. Stand. 49 (1952) 409.
[37] A. Kashinath, A. Misra, M.J. Demkowicz, Phys. Rev. Lett. 110 (2013) 086101.
[38] M. Demkowicz, R. Hoagland, J. Hirth, Phys. Rev. Lett. 100 (2008) 136102.
[39] D.L. Olmsted, S.M. Foiles, E. a. Holm, Acta Mater. 57 (2009) 3694.
[40] T. Korhonen, M.J. Puska, R.M. Nieminen, Phys. Rev. B 51 (1995) 9526.
[41] P. Ehrhart, P. Jung, H. Schultz, Atomic Defects in Metals, Springer Berlin Heidelberg, 1991.
[42] H.E. Schaefer, Phys. Status Solidi A-Applied Res. 102 (1987) 47.
[43] L. Pizzagalli, M.-L. David, J. Deres, Phys. Status Solidi A (2017) 1700263.
[44] M.J. Puska, S. Poykko, M. Pesola, R.M. Nieminen, Phys. Rev. B 58 (1998) 1318.
[45] S. Dannefaer, P. Mascher, D. Kerr, Phys. Rev. Lett. 56 (1986) 2195.
[46] A.K. Bandyopadhyay, S.K. Sen, Phys. Status Solidi 157 (1990) 519.
[47] L. Kornblit, Phys. Rev. B 22 (1980) 1866.
[48] N.Q. Lam, L. Dagens, N. V Doan, J. Phys. F Met. Phys. 13 (1983) 2503.
[49] P. Rinke, A. Janotti, M. Scheffler, C.G. Van De Walle, Phys. Rev. Lett. 102 (2009) 1.
[50] Y. Wang, A.H. MacDonald, Phys. Rev. B 52 (1995).
[51] M.J. Demkowicz, J. Wang, R.G. Hoagland, Dislocations in Solids 14 (2008) 141.
[52] W.H. Zachariasen, J. Am. Chem. Soc. 54 (1932) 3841.
[53] Y.Q. Cheng, E. Ma, Prog. Mater. Sci. 56 (2011) 379.
[54] J. Fortner, J.S. Lannin, Phys. Rev. B 39 (1989) 5527.
[55] S. Zhao, E.N. Hahn, B. Kad, B.A. Remington, C.E. Wehrenberg, E.M. Bringa, M.A. Meyers, Acta

Mater. 103 (2016) 519.
[56] D.L. Williamson, S. Roorda, M. Chicoine, R. Tabti, P.A. Stolk, S. Acco, F.W. Saris, Appl. Phys. Lett. 67 (1995) 226.
[57] D.N. Seidman, R.S. Averback, P.R. Okamoto, A.C. Baily, Phys. Rev. Lett. 58 (1987) 900.
[58] R.E. Baumer, M.J. Demkowicz, Acta Mater. 83 (2015) 419.
[59] X. Liu, B.E. White Jr., R.O. Pohl, E. Iwanizcko, K.M. Jones, A.H. Mahan, B.N. Nelson, R.S. Crandall, S. Veprek, Phys. Rev. Lett. 78 (1997) 4418.
[60] B.N. Singh, Philos. Mag. 29 (1974) 25.
[61] W.S. Yu, M.J. Demkowicz, J. Mater. Sci. 50 (2015) 4047.
[62] S. Von Alfthan, P.D. Haynes, K. Kaski, A.P. Sutton, Phys. Rev. Lett. 96 (2006).
[63] M. Demkowicz, R. Hoagland, J. Hirth, Phys. Rev. Lett. 100 (2008) 136102.
[64] S. Roorda, W.C. Sinke, J.M. Poate, D.C. Jacobson, S. Dierker, B.S. Dennis, D.J. Eaglesham, F. Spaepen, P. Fuoss, Phys. Rev. B 44 (1991) 3702.
[65] W. Kauzmann, Chem. Rev. 43 (1948) 219.
[66] C.A. Angell, J. Non. Cryst. Solids 354 (2008) 4703.
[67] J.K. Krüger, K.P. Bohn, R. Jiménez, J. Schreiber, Colloid Polym. Sci. 274 (1996) 490.
[68] E.J. Sare, C.A. Angell, J. Solution Chem. 2 (1973) 53.
[69] W.Z. Han, M.J. Demkowicz, E.G. Fu, Y.Q. Wang, A. Misra, Acta Mater. 60 (2012) 6341.
[70] M.J. Demkowicz, A. Misra, A. Caro, Curr. Opin. Solid State Mater. Sci. 16 (2012) 101.
[71] M.A. Tschopp, K.N. Solanki, F. Gao, X. Sun, M.A. Khaleel, M.F. Horstemeyer, Phys. Rev. B - Condens. Matter Mater. Phys. 85 (2012).
[72] M.J. Demkowicz, O. Anderoglu, X. Zhang, A. Misra, J. Mater. Res. 26 (2011) 1666.
[73] A. Vattré, T. Jourdan, H. Ding, M.-C. Marinica, M.J. Demkowicz, Nat. Commun. 7 (2016) 10424.
[74] W. Han, M.J. Demkowicz, N.A. Mara, E. Fu, S. Sinha, A.D. Rollett, Y. Wang, J.S. Carpenter, I.J. Beyerlein, A. Misra, Adv. Mater. 25 (2013) 6975.
[75] C. Brandl, T.C. Germann, A. Misra, Acta Mater. 61 (2013) 3600.
[76] L. Yang, H.Y. Li, P.W. Wang, S.Y. Wu, G.Q. Guo, B. Liao, Q.L. Guo, X.Q. Fan, P. Huang, H.B. Lou, F.M. Guo, Q.S. Zeng, T. Sun, Y. Ren, L.Y. Chen, Sci. Rep. 7 (2017).
[77] T. Egami, K. Maeda, V. Vitek, Philos. Mag. A 41 (1980) 883.
[78] J.F. Joly, L.K. Béland, P. Brommer, N. Mousseau, Phys. Rev. B - Condens. Matter Mater. Phys. 87 (2013).